Quantum storage of entangled photons at telecom wavelengths in a crystal

Ming-Hao Jiang, 1, * Wenyi Xue, 1, * Qian He, 1 Yu-Yang An, 1 Xiaodong Zheng, 1 Wen-Jie Xu, 1 Wenjun Wen, 1 Yu-Bo Xie, 1 Yanqing Lu, 1 Shining Zhu, 1 and Xiao-Song Ma 1,2,3,†

¹National Laboratory of Solid-state Microstructures, School of Physics, College of Engineering and Applied Sciences, Collaborative Innovation Center of Advanced Microstructures, Nanjing University, 210093 Nanjing, China ²Synergetic Innovation Center of Quantum Information and Quantum Physics, University of Science and Technology of China, Hefei, Anhui 230026, China ³Hefei National Laboratory, Hefei 230088, China (Dated: December 27, 2022)

The quantum internet 1,2 — in synergy with the internet that we use today — promises an enabling platform for next-generation information processing, including exponentially speed-up distributed computation, secure communication, and high-precision metrology. The key ingredients for realizing such a global network are the distribution and storage of quantum entanglement $^{3-7}$. As ground-based quantum networks are likely to be based on existing fibre networks, telecom-wavelength entangled photons and corresponding quantum memories are of central interest. Recently, $^{167}\rm{Er}^{3+}$ ions have been identified as a promising candidate for an efficient, broadband quantum memory at telecom wavelength⁸. However, to date, no storage of entangled photons, the crucial step of quantum memory using these ions, has been reported. Here, we demonstrate the storage and recall of the entangled state of two telecom photons generated from an integrated photonic chip based on silicon nitride. Combining the natural narrow linewidth of the entangled photons and long storage time of $^{167}\rm{Er}^{3+}$ ions, we achieve storage time of 400 ns, more than one order of magnitude longer than in previous works. Successful storage of entanglement in the crystal is certified by a violation of an entanglement witness with more than 12 standard deviations (-0.161 \pm 0.012) at 400 ns storage time. These results pave the way for realizing quantum networks based on solid-state devices.

INTRODUCTION

For fibre-based quantum networks, the distance over which entanglement can be distributed is limited to around 100 km, due to losses in the optical fibre. The quantum-communication efficiency can be greatly enhanced, however, by harnessing quantum-repeater architectures³⁻⁷. The key building block of such architectures is quantum memory, wherein photonic quantum states are stored in quantum states of matter. Quantum memories have been realized with atomic ensembles⁹⁻¹³, single atoms¹⁴⁻¹⁷ and solid-state systems¹⁸⁻²⁷. For the integration of these elements into a quantum network, three general criteria have to be met⁷: 1. wavelength compatibility with existing telecom networks (i.e., the natural choice for the level transition in the storage device should be around 1.5 μ m for low propagation loss); 2. long storage times; and 3. multiplexed storage capability. One of the most promising candidates for realizing such a memory are solids doped with rare-earth ions. Several recent experiments with non-Kramers ions (that is, ions with an even number of electrons), such as praseodymium or europium, have established the potential to realize practical memories by demonstrating storage in long-lived spin states^{28–30}, multimode storage^{30,31}, high efficiencies^{32,33} and long storage times^{34,35}. These successful demonstrations built on the long ground-state hyperfine lifetimes in these ions, which enable efficient optical pumping for high-fidelity initial-state preparations and long hyperfine coherence times. These are inherent properties of non-Kramers ions, as the crystal field for sites with sufficiently low symmetry quenches the electronic angular momenta of these ions. They are essential for realizing an efficient, long-lived quantum memory. However, none of the non-Kramers ions have suitable optical transitions in any of the telecom bands; nonetheless, flying photon at telecom wavelength can be realized either by frequency conversion 11,36-38 or entanglement heralding with frequency non-degenerate photon-pair sources 19,20,39-41.

The erbium ion, a Kramers ion, has an optical transition in the telecom band around 1,530 nm. However, the odd number of electrons — and therefore half-integer spin — of Er ions means that optical pumping of the ground-state electron-spin levels is inefficient, as the magnetic moment of Kramers ions cannot be quenched by a crystal field. Previous studies towards developing quantum memories using erbium have suffered from this shortcoming. Entangled states⁴² and non-classical states⁴³ of light have been stored in Er-doped glass fibre with an efficiency of \sim 1% and storage times of 5-50 ns, and in a crystal waveguide with an efficiency of \sim 0.1% and a storage time of around 50 ns⁴⁴. Moreover, a two-level gradient-echo memory technique was employed to store weak coherent states in a crystal, with a reported efficiency of $0.25\%^{45}$.

Rančić et al.⁸ recently showed that in a high magnetic field, $^{167}\text{Er}^{3+}$ ions with I=7/2 possess a hyperfine coherence time of 1.3 s and efficient spin pumping of the ensemble into a single hyperfine state. This seminal work triggered

a recent resurgence of interest in using erbium for quantum memory, for example for on-chip storage of telecomband light at the single-photon level⁴⁶, for efficient initialization using the resolved hyperfine structure for quantum memories⁴⁷, and for on-demand storage with laser-written waveguides⁴⁸. The next milestone of quantum memory in this system is to store quantum entanglement in ¹⁶⁷Er³⁺ ions and show that entanglement is preserved after storage. Our work achieves this goal by implementing following steps: 1. We create a pair of entangled (signal and idler) photons, both of which at wavelengths in the telecom C-band; 2. we initialize the ¹⁶⁷Er³⁺ quantum memory and then send the signal photon into the memory for storage; 3. after storage, the signal photon is released from the memory; and 4. we analyze the correlation between the released signal photon and the idler photon, which has not been stored, and verify the entanglement with the quantum memory.

EXPERIMENT AND RESULTS

A schematics of our experimental set-up is shown in Fig. 1 (see the SI for details). The set-up consists of an entanglement source, a quantum memory and an entanglement analyzer. The time-bin entangled photon pairs are generated from an integrated silicon nitride (SiN)^{49–56} dual Mach–Zehnder interferometer micro-ring (DMZI-R) resonator⁵⁷⁻⁶⁰, which uses the spontaneous four-wave mixing (SFWM) process(inset of Fig. 2b). The output of a continuous-wave pump laser (CW1) is chopped by an intensity modulator into pulses. These pulses are then further amplified with an erbium-doped fibre amplifier (EDFA). Several wavelength-division multiplexers (WDM) are used to clean the spectrum of the pulses, which are subsequently injected into the 'In' port of the SiN DMZI-R resonator (Fig. 2a). A pair of telecom-wavelength photons that are not degenerate in frequency, signal and idler photons, are generated from the resonator and coupled out from the 'Drop' port. In the ideal case, all the signal and idler photons generated in the DMZI-R are extracted from the 'Drop' port and are then coupled out from the chip. Signal and idler photons are then separated with a WDM. The remaining pump pulses are coupled out from the 'Through' port (T) and detected with a photodiode (PD). We use the detected power signal to monitor the frequency drift between the resonance of the DMZI-R and the pump⁵⁶. The additional 'Add' port is used for calibrating the DMZI-R resonance conditions. The unique structure of the DMZI-R source allows us to independently tune the coupling between the waveguide and ring resonator for the pump pulses, signal and idler photons. In this way, we achieve the critical coupling for the pump light to achieve efficient photon-pair generation in the resonator and to reduce the on-chip and in-fibre Raman noise generated from the strong pump. Simultaneously, we also achieve over-coupling of both signal and idler photons to reduce the unwanted propagation loss in the resonator ^{57–60}. The SiN DMZI-R resonator chip is optically and electrically packaged for long-time stable operation.

The transmission spectrum of this DMZI-R source is shown in Fig. 2b. The quality factors of the signal (1536.17 nm), pump (1538.52 nm) and idler (1540.87 nm) wavelengths are around 5.5×10^5 , 9.7×10^5 and 3.4×10^5 , respectively. Cavity-enhanced SFWM processes enable us to generate high-quality telecom entangled photons with high brightness and narrow linewidth, which are the essential requirements for telecom-compatible quantum memory. Fig. 2c shows the coincidence histogram for a 2-mW pulsed pump, with a coincidence window of about 4 ns. The full width at half maximum (FWHM) of the coincidence peak is 622 ps, which corresponds to a coherence time of 342 ps and 555 ps for the idler and signal photons, respectively 61,62 (see SI for details). These single-photon results are consistent with the linewidth of the classical transmission spectrum. We further measure the coincidence counts (C.C.) rate and the coincidence-to-accidental ratio (CAR) as a function of pump average power with continuous wave (CW) and pulsed pump, shown in Fig. 2d and Fig. 2e, respectively. When we increase the pump power, due to the nature of SFWM, on one hand, we observe the enhancement of coincidence counts; on the other hand, high-order photon pairs reduce the CAR.

In the pulsed-pump case, the output of laser CW1 is chopped with an intensity modulator into pulses with a 4-ns pulse duration and a 32-ns period. By using these pump pulses, we generate time—bin entangled qubit state:

$$|\Phi\rangle = |ee\rangle + |ll\rangle,\tag{1}$$

in which $|e\rangle$ and $|l\rangle$ represent early and late temporal modes of the single photons, respectively. Photon pairs generated by the DMZI-R are time—bin entangled and the pair-creation time is uncertain within the coherence time of the pump laser. In order to analyze the two-photon entanglement, we send them into two Franson interferometers⁶³. Each interferometer has two unbalanced optical paths, where the temporal difference between two optical paths is approximately 32 ns. Note that there are two time parameters that need to be treated carefully: the first one is the time difference between optical paths of one interferometer, ΔT , which needs to match the period of the pump pulses and be larger than the single-photon coherence time; the second one is the difference between this parameter for two interferometers, $\Delta T_1 - \Delta T_2$, which needs to be smaller than the coherence time of the signal and

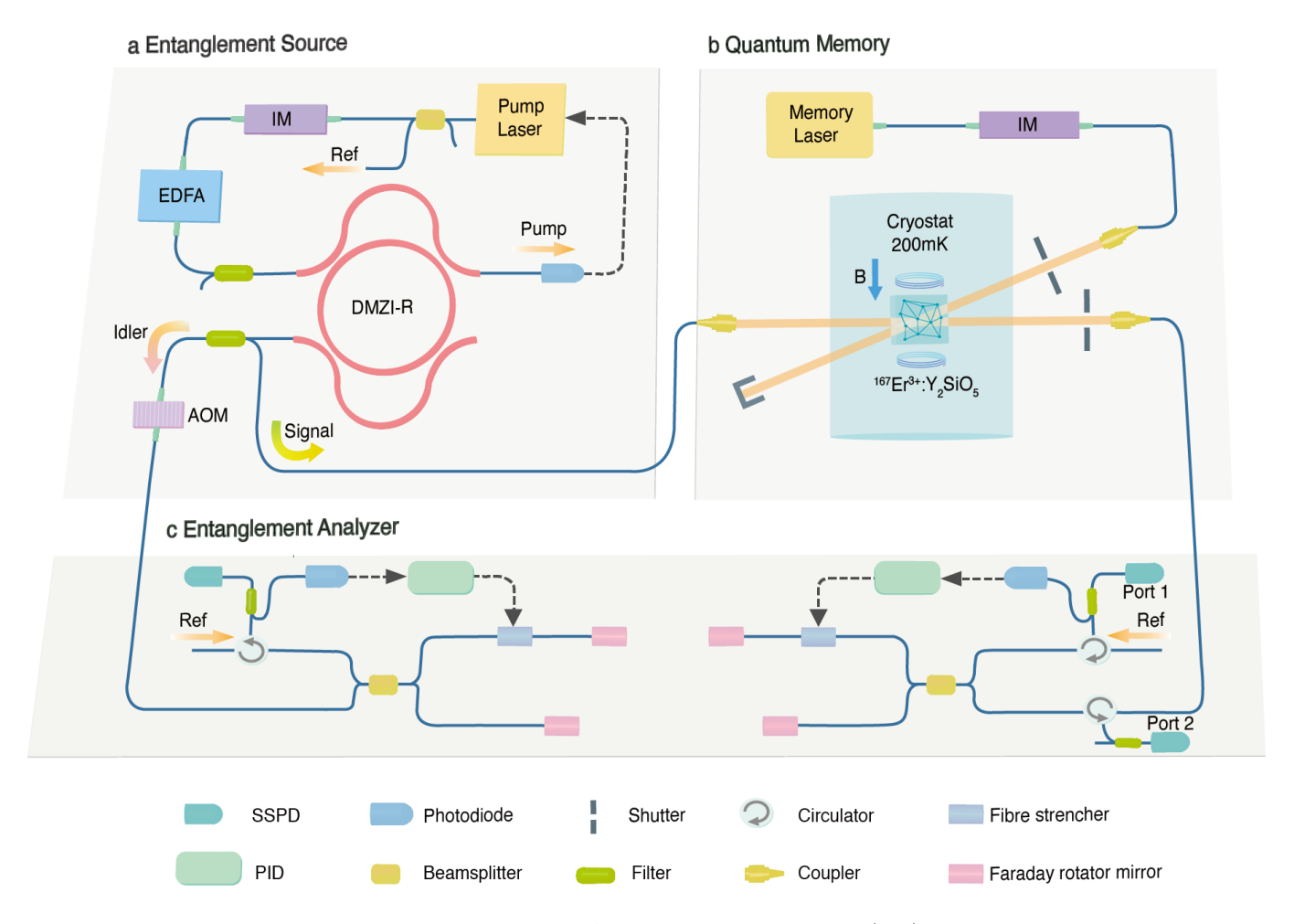


FIG. 1. Schematics of the experimental set-up. a. An integrated silicon nitride (SiN) dual Mach–Zehnder interferometer micro-ring resonator (DMZI-R) generates time–bin entangled photon pairs via spontaneous four-wave mixing process. See text for details. b. Quantum memory based on $^{167}\mathrm{Er}^{3+}$:Y₂SiO₅. The 1536.17 nm continuous-wave memory laser is modulated with an intensity modulator (IM). The memory $^{167}\mathrm{Er}^{3+}$:Y₂SiO₅ crystal is cooled to about 200 mK in a dilution refrigerator and exposed to a 1.5-T magnetic field aligned in the D_1 - D_2 plane of the crystal with an angle of about $\theta = 120^{\circ}$ to the D_1 axis. A pair of optical shutters are used to control the time sequence of signal photon and memory laser. c. Time–bin qubit entanglement analyzer. We send the signal photon to the quantum memory and then to a Franson interferometer. The idler photon is sent to a Franson interferometer directly. Both interferometers are phase stabilized with proportional-integral-derivative (PID) controllers by using a fraction of pump laser as reference light (Ref), and analyze the entanglement between both photons. See text and SI for details.

idler photons. We fulfill both requirements by adjusting the pump-pulse period and accurate fibre splicing for both Franson interferometers. We scan the relative phases of the two unbalanced interferometers by tuning the setpoints of the two proportional—integral—derivative (PID) phase-locking systems for them, and obtain the two-photon quantum interference for the full 2π period, as shown in Fig. 2f. For entanglement analysis, we use the average pulsed pump power of about 4 mW, where the CAR decreases to about 8. The visibilities ($V = \frac{\text{max-min}}{\text{max+min}}$) for these two curves are 77.5 \pm 0.6% and 73.6 \pm 0.6%, which are above the limit of $1/\sqrt{2} \approx 70.7\%$ required to violate the Clauser–Horne–Shimonv–Holt (CHSH) version of Bell inequalities⁶⁴.

The quantum memory is a 50 ppm doped $^{167}\mathrm{Er}^{3+}$: $Y_2\mathrm{SiO}_5$ crystal, which is cut along its D_1 , D_2 and b axes with dimensions of $4\times5\times9$ mm³. A photon-echo-type interaction using an atomic frequency comb (AFC)⁶⁵ enables the quantum state to transfer between the single photon and the atomic ensemble. To create an AFC, we use the optical pumping technique to shape the absorption profile of the atomic ensemble into a comb-like structure. The input photon is then absorbed and re-emitted into a well-defined spatial mode because of a collective rephasing of the atoms in the AFC. The period of the comb determines the re-emission time and can be reconfigured.

Here we use the $^{167}{\rm Er^{3+}}$ ions at site 1, with the $^4{\rm I}_{15/2} \rightarrow {}^4{\rm I}_{13/2}$ transition at ~ 1536.17 nm. In addition to Zeeman

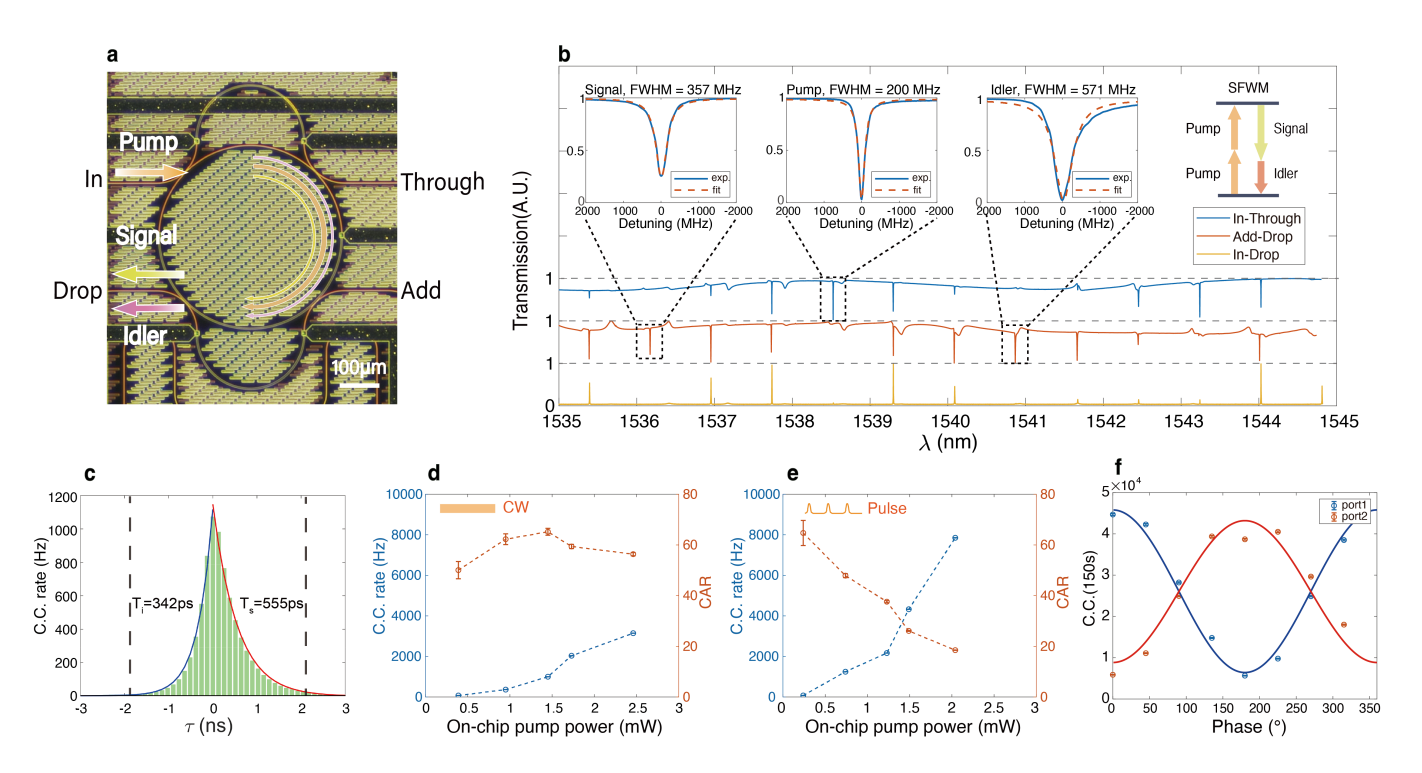


FIG. 2. Entangled photon-pair source based on integrated photonics. a. Optical micrograph of the integrated silicon nitride (SiN) dual Mach–Zehnder interferometer micro-ring resonator (DMZI-R) for generating pairs of time—bin entangled photons. b. Transmission spectra of the SiN DMZI-R source for In–Through, Add–Drop and In–Drop as input–output ports, shown in blue, red and yellow, respectively. Insets: The experimental spectra (blue) and the fitting Lorentzian functions (red) for the signal, pump and idler photons. Their full widths at half maximum (FWHM) are about 357 MHz, 200 MHz and 571 MHz, respectively. Two identical pump photons generate a pair of frequency non-degenerate signal and idler photons via the spontaneous four-wave mixing process. c. Typical coincidence histogram with a 2-mW pulsed pump, shows an asymmetric feature, resulting from different linewidths of signal and idler photons. The left and right decay times are around 342 ps and 555 ps, respectively. We choose 4 ns as the coincidence window, indicated with two dashed vertical lines. d/e. The coincidence counts (C.C.) rate and coincidence-to-accidental ratio (CAR) for continuous wave (CW)/pulsed pump (with 4-ns on-time and 32-ns period) as a function of average pump power. (f) Two-photon coincidence counts as a function of the relative phase between two Franson interferometers. The blue/red circles are the raw data for coincidence counts between idler and port 1/2 of the signal photon, respectively. Their visibilities surpass the CHSH threshold of 70.7%. See text for details. Error bars are derived from Poissonian statistics and error propagation.

splitting, $^{167}\text{Er}^{3+}$ exhibits eight hyperfine spin states due to a nuclear moment of I=7/2 (see Fig. 3a). The crystal is placed inside a dilution refrigerator integrated with a superconducting magnet. The pump laser and signal photons propagate along the b axis. A magnetic field of 1.5 T is applied in the D_1 - D_2 plane with an angle of about $\theta=120^\circ$ to the D_1 axis for a maximal ground-state Zeeman splitting. The crystal temperature is around 200 mK, deduced from the thermal-equilibrium population between Zeeman ground levels in different magnetic fields (see SI for details). In this case, the ground-state Zeeman splitting is about 60 times k_BT , so that the electron spin is frozen to $m_e=-1/2$, ensuring long lifetimes and coherence times⁸.

The inhomogeneous broadening of our sample is larger than the hyperfine splitting, which means that the transitions of $\Delta m_I = \pm 1$ and $\Delta m_I = 0$ cannot be resolved. We use a simplified spin Hamiltonian to model the hyperfine structure of this system, and obtained consistent results with the experimental spectral hole burning (SHB) data (see SI for details). In our experiment, the magnetic field slightly deviates from the D_1 - D_2 plane, lifting the degeneracy of the two classes of $^{167}{\rm Er}^{3+}$ ions. To create the desired AFC profiles, we modulate the intensity of the pump laser into pulses with a duration of around 6 ns and a period equal to the storage time $t_{\rm M}$, so that its frequency spectrum will be a comb with $1/t_{\rm M}$ period modulated by a sinc function whose main peak spans about 333 MHz. The experimental spectra of the full inhomogeneous broadening is shown in Fig. 3b. A zoomed-in view is shown in Fig. 3c, compared with the spectral line-shape of the input signal photon. The relative detunings of anti-holes and side-holes are similar to those of a single SHB (see SI for details). The anti-holes close to the pump frequency enhance the absorption between AFC teeth. In Fig. 3d–f, we show zoomed-in views of the AFC-preparation profiles with different storage time ($t_{\rm M}$). For storage time of 80 ns, 240 ns and 400 ns, the AFC structure is set with a frequency spacing of 12.5

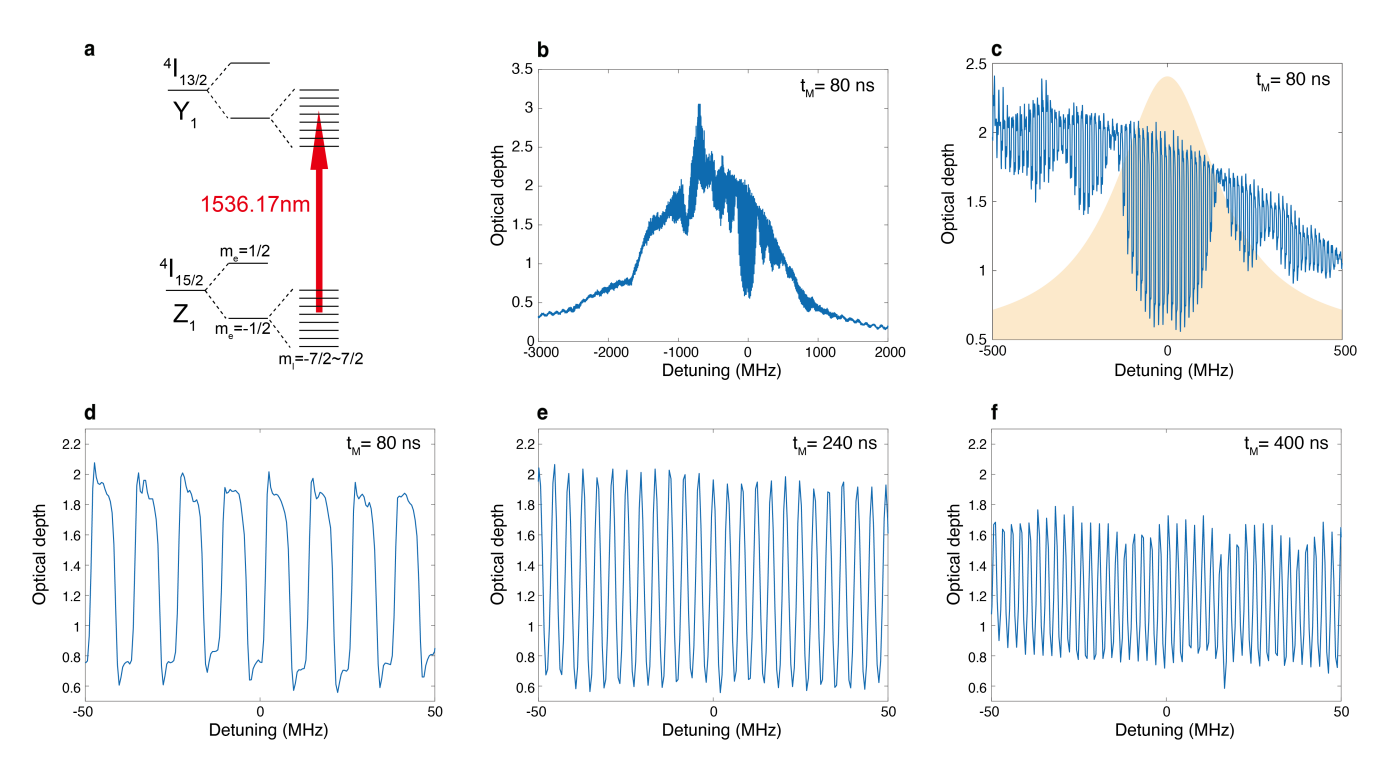


FIG. 3. An atomic-frequency-comb (AFC) quantum memory based on a $^{167}\mathrm{Er^{3+}}$:Y₂SiO₅ crystal. a. The energy level diagram of $^{167}\mathrm{Er^{3+}}$:Y₂SiO₅. b. The full absorption spectrum after AFC preparation. c. The AFC spectrum with a bandwidth of around 333 MHz for the central structure matches the spectrum of the input signal photon (orange). In panels d, e and f, we show the zoom-in of the profile of AFC preparation with the storage time of 80 ns, 240 ns and 400 ns, respectively. The AFC structure is set with a frequency spacing of 12.5 MHz, 4.16 MHz and 2.5 MHz, with a finesse of \sim 2.

MHz, 4.16 MHz and 2.5 MHz, respectively, with a constant finesse of \sim 2 realized by correspondingly sweeping the memory laser.

In order to store the heralded single photon, we align the frequency of the signal photon with respect to that of the quantum memory. To achieve that, we first tune the frequency of the photon-pair source by adjusting the temperature of the DMZI-R source. The DMZI-R resonance is sensitive to temperature, which is measured with a negative-temperature-coefficient thermistor, and stabilized with a thermoelectric cooler with feedback control. The pump wavelength is locked to the resonance of the DMZI-R with a feedback loop by monitoring the remaining pump power at the through port. Another knob we have is the magnetic field applied to the quantum memory. We vary the magnetic-field amplitude to tune the Zeeman splitting and hence the optical transition frequency of ¹⁶⁷Er³⁺ ions. We present a typical result for the frequency alignment in Fig. 4a. We show the single counts (S.C.) of the signal (blue) and idler (red) photons as a function of the magnetic-field amplitude. The clear drop of counts of signal photon shows the matching of the absorption frequency of the memory with respect to that of the signal photon. However, it is also important to have a stable count rate for idler photon, as the drop of signal-photon counts can also come from the drift of the pump laser with respect to the DMZI-R. Only by observing the drop of signal-photon counts and, simultaneously, the constant idler-photon counts, can we be certain that frequency alignment of the resonance of ¹⁶⁷Er³⁺ ions and the signal photon has been achieved. For a more precise alignment of signal photon to the AFC, we scan the temperature of the DMZI-R in finer steps to tune the frequency of the signal photon for achieving maximal storage efficiency, with the magnetic field fixed to 1.5 T (see SI for details). We employ another feedback loop to keep the ratio of counts of signal to idler photons constant for long-term stability (see Fig. 4b). Note that the ratio in Fig. 4b is not equal to that in Fig. 4a because the DMZI-R temperature has changed for further optimizations, as mentioned above.

After achieving the frequency alignment, we proceed with storage of the heralded signal photons. Two optical shutters are employed to protect the superconducting single-photon detectors (SSPD) from the memory laser, with a 3.7 s AFC preparation window, a 1 s memory window and a delay of 200 ms in between. An acousto-optic modulator (AOM) is inserted to gate the idler photons in synchronization with the memory window. In Fig. 4c, we show the coincidence histograms for different predetermined storage times (80 ns, 240 ns and 400 ns). The 32-ns period of the

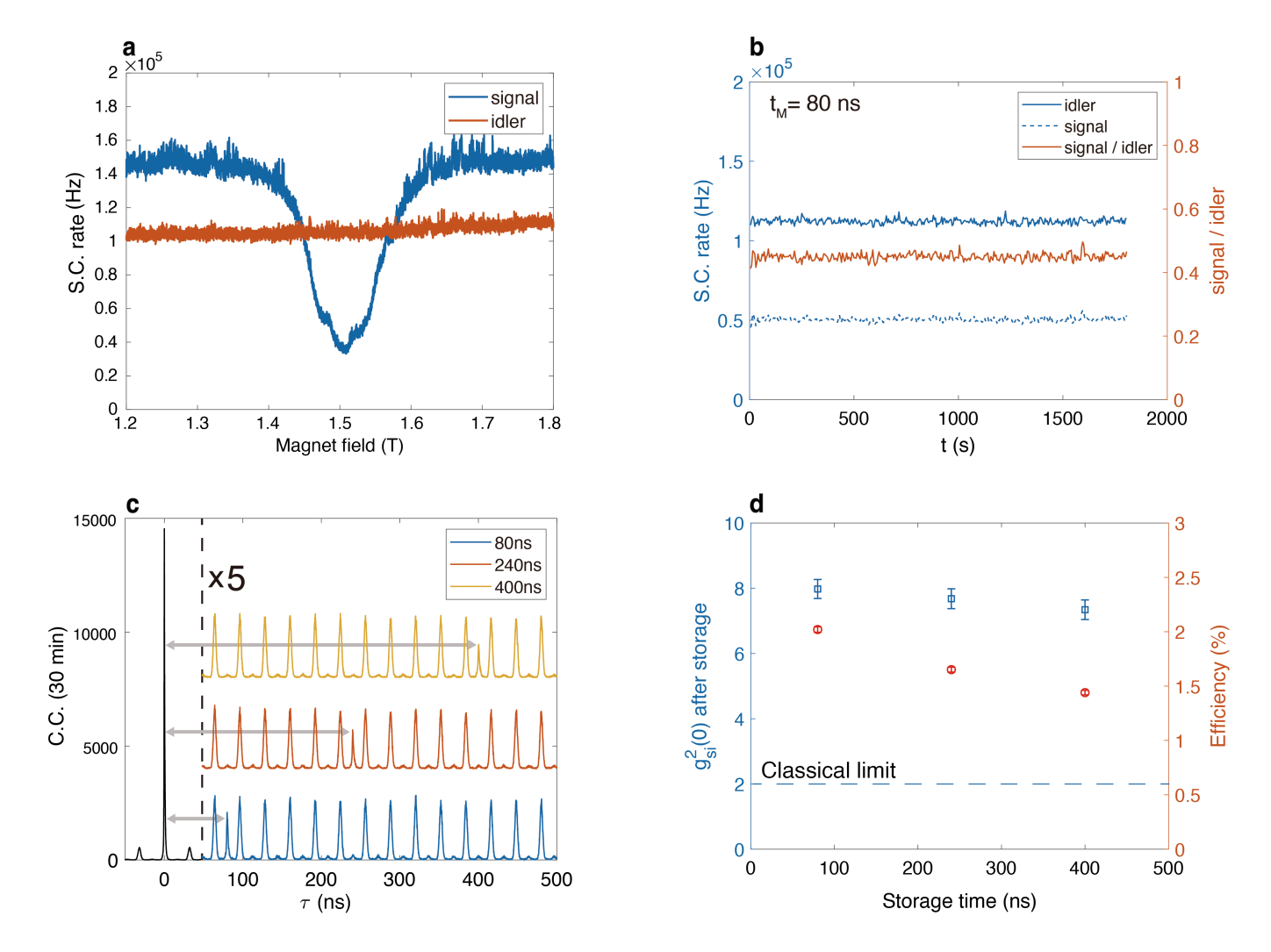


FIG. 4. Quantum storage of the heralded single photon in an $^{167}{\rm Er}^{3+}$:Y₂SiO₅ crystal. a. Frequency alignment between the input-signal photon and the absorption of $^{167}{\rm Er}^{3+}$ ions. The single counts (S.C.) of the signal (blue) and idler (red) photons are shown as a function of the magnetic-field amplitude. The clear drop of the counts of signal photon shows the matching of the absorption frequency of the memory with respect to that of the signal photon. b. Long-term stability of the frequency alignment with feedback control. The single counts of signal, idler photons and their ratio are stabilized over long time, enabling long-term operation of our experiment. c. The coincidence counts (C.C.) histograms for different storage times: 80 ns (blue), 240 ns (red) and 400 ns (yellow), vertically offset for clarity. The 32 ns period of the side peaks reflect the period of the pump laser, creating accidental coincidence counts. The data beyond 48 ns are magnified by a factor of five. d. Blue squares: for storage times up to 400 ns, the second-order correlations stay well above the classical limit, $g_{\rm si}^2(0) = 2$. Red circles: the efficiencies for different storage times. Error bars are derived from Poissonian statistics and error propagation.

side peaks is due to the periodic pulses of the pump laser, which creates accidental coincidence (AC) counts. The cross-correlation function is calculated as $g_{\rm si}^2(0) = \frac{p_{\rm si}}{p_{\rm s}p_{\rm i}}$, where $p_{\rm si}$ is the probability of coincidence detections of idler and signal photons, and $p_{\rm s}$ ($p_{\rm i}$) is the probability of single clicks of signal (idler) photons, respectively. As shown in Fig. 4d, the cross-correlation remains well above the classical bound of thermal light, $g_{\rm si}^2(0) = 2^{66,67}$. The memory efficiencies for various storage times are also shown in Fig. 4d, indicating an efficiency of ~1.4% for 400 ns storage. Note that all results presented in this article are without any subtraction of background noise or AC counts.

The maximum number of temporally multiplexed modes is approximately equal to the time—bandwidth product $(TBP)^{65}$, which is the storage time divided by the time width of the stored photons. In this work, the TBP is about 400 ns/4 ns = 100. However, the realized mode number is 12, with 32 ns repetition time and 400 ns storage time. The main limitation here is the 32 ns repetition time, which is equal to the time difference of each unbalanced interferometer and should be larger than the single-photon coherence time, as discussed before. This can be solved by either coding the qubits on other degrees of freedom, or still using time—bin qubits but with a dense coding method. In

TABLE 1. Two-fold coincidence visibility (V), the second-order correlation function $(g_{si}^2(0))$, and the expectation value of the
entanglement witness $(\langle W \rangle)$ for different storage time $(t_{\rm M})$. The coincidence is between the idler photon and one of output
ports of the signal photon, port $1/2$, see Fig. 1.

$\overline{t_{ m M}}$	Signal port	V	$g_{ m si}^2(0)$	$\langle W angle$
80	1	$68.3 \pm 1.8\%$	7.977 ± 0.292	-0.241 ± 0.0095
00	2	$69.8 \pm 1.9\%$		-0.249 ± 0.0099
240	1	$67.9 \pm 1.8\%$	7.680 ± 0.305	-0.236 ± 0.0096
240	2	$65.7\pm1.9\%$		-0.225 ± 0.0100
400	1	$64.0\pm2.3\%$	7.342 ± 0.301	-0.213 ± 0.0120
400	2	$53.5\pm2.4\%$		-0.161 ± 0.0125

this way, the 'early' mode of N time—bin qubits come in order before the the 'late' mode of the first qubit, enhancing the mode capability by a factor of N^{68} .

After showing the storage of the heralded single photon, we now present the entanglement-storage results, in which the entanglement of the photon pair is preserved after the signal photon has been stored in the crystal. To do so, we sent the stored and re-emitted signal photon and the not-stored idler photon into the entanglement analyzer (Fig. 1), consisting of two unbalanced interferometers, for performing the Franson-type quantum interference experiment. In Fig. 5a, we show the histogram of coincidence between output port 1 for the signal photon and the output port for the idler photon. There are five peaks spanning from 40 to 120 ns. The central peak corresponds to the quantum interference peak of the entangled state (Eq. 1). By setting the relative phase of the two unbalanced interferometers in the entanglement analyzer to 0 and π , we observe fully constructive and destructive interference. In Fig. 5b, the coincidence between output port 2 for the signal photon and the output port for the idler photon is reversed for the same phase setting as in Fig. 5a. This is due to the complementary properties of the interferometers. In addition, the outmost two peaks in Fig. 5a,b are phase insensitive, as they correspond to the $|el\rangle$ and $|el\rangle$ coincidence counts, which are distinguishable in time. The other two peaks are the accidental coincidence peaks mentioned above. Furthermore, we scan the relative phase of the two unbalanced interferometers by tuning the setpoints of the two PID phase-locking systems, and obtain two-photon quantum interference for the full 2π period at 80 ns storage time, as shown in Fig. 5c. The visibilities for these two curves are $68.3 \pm 1.8\%$ and $69.8 \pm 1.9\%$, respectively. The same experiment is performed with 240 ns and 400 ns storage time for the relative phase of 0 and π , with results for 400 ns storage time shown in Fig. 5d,e. The data was integrated for 3 hours, and the single counts of signal and idler photons is shown in Fig. 5f, demonstrating the long-term stability of our experiment.

An entanglement witness⁶⁹ is employed to determine whether entanglement exists. Existence of entanglement is proved by determining a negative expectation value of the witness operator. The witness used here is given by

$$\hat{W} = \frac{1}{2} (|z^{+}z^{-}\rangle\langle z^{+}z^{-}| + |z^{-}z^{+}\rangle\langle z^{-}z^{+}| + |x^{+}x^{-}\rangle\langle x^{+}x^{-}| + |x^{-}x^{+}\rangle\langle x^{-}x^{+}| - |y^{+}y^{-}\rangle\langle y^{+}y^{-}| - |y^{-}y^{+}\rangle\langle y^{-}y^{+}|),$$
(2)

where $|z^{+}\rangle = |e\rangle$, $|z^{-}\rangle = |l\rangle$, $|x^{\pm}\rangle = |e\rangle \pm |l\rangle$ and $|y^{\pm}\rangle = |e\rangle \pm i|l\rangle^{70}$. Projections onto the X–Y plane can be obtained from the visibility of the Franson interference. Combined with the results for Z basis (Fig. 4c,d) when the unbalanced interferences are removed, the expectation value of the witness can be calculated using:

$$\langle W \rangle = \frac{1}{g_{\rm si}^2(0) + 2} - \frac{V}{2}.$$
 (3)

The entanglement witnesses with different storage times are shown in Tab. 1, where all values are below the separable boundary of 0, by more than 12 standard deviations. Therefore, our results unambiguously show the successful storage of entangled photons in a crystal for 400 ns.

CONCLUSIONS

Our results represent a significant advancement of quantum memory system. First, we show the storage of entangled photons in $^{167}\mathrm{Er^{3+}}$: $\mathrm{Y_{2}SiO_{5}}$, a quantum memory at telecom wavelength, which is a promising candidate for realizing

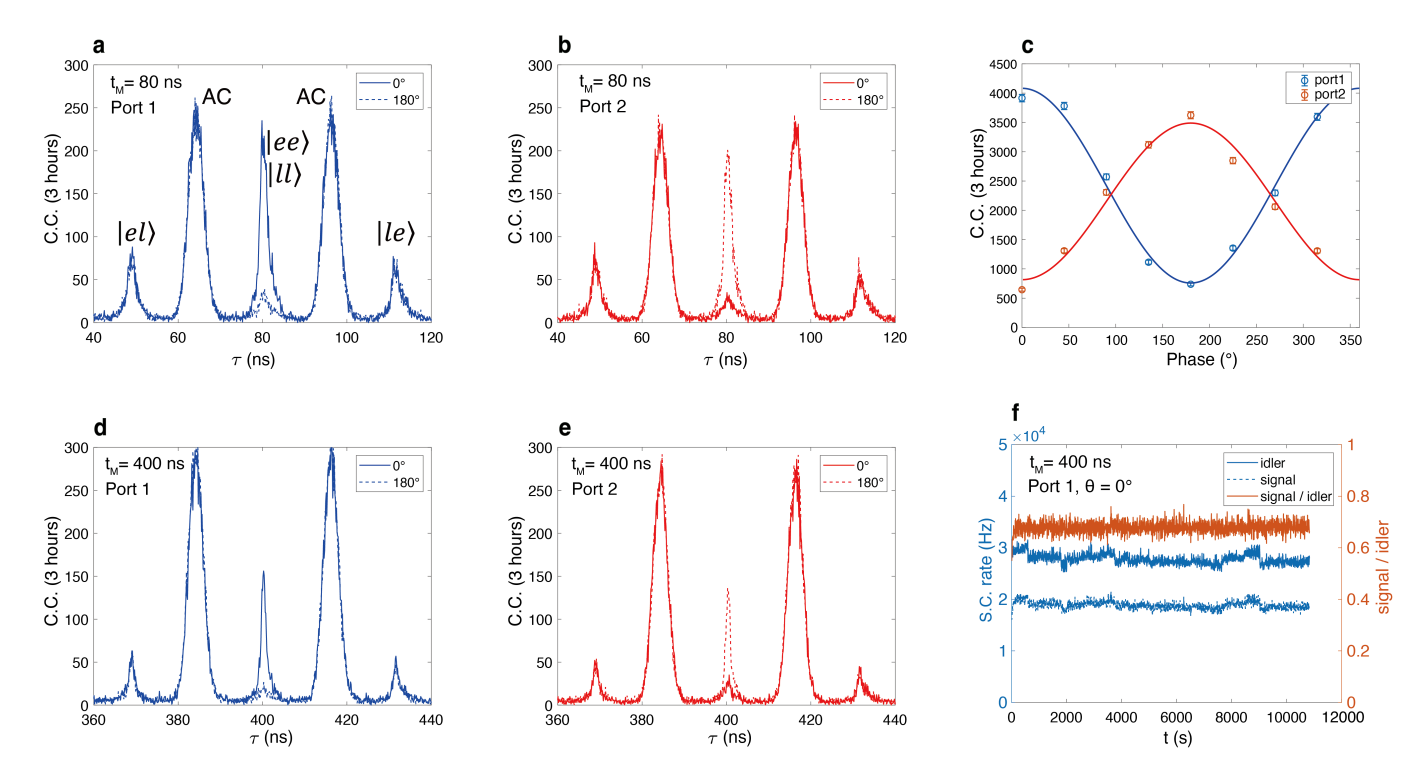


FIG. 5. Quantum storage of entanglement. a. After a storage time of 80 ns, the signal photon is re-emitted from the quantum memory. By using two Franson interferometers for the re-emitted signal photon and the not-stored idler photon, we select the central peak (at 80 ns) to verify the entanglement between them. The coincidence counts between idler photons and port 1 of the Franson interferometer for signal photons are shown in solid/dashed blue curves for a relative phase of $0/180^{\circ}$, respectively. b. The coincidence counts between idler photons and port 2 of the Franson interferometer for signal photons are shown in solid/dashed red curves for the relative phase of $0/180^{\circ}$, respectively. Complementary counts at the same phase setting are clearly seen from in panels a and b, as expected for interferometric measurements. c Full-period interference fringes show the coherence of the entangled state of Eq. 1. We scan the relative phase of the two Franson interferometers and obtain two-photon quantum interference for the full 2π period. The coincidence counts between port 1/2 of the Franson interferometer for signal photons and idler photons are shown in blue/red curves, respectively. Error bars are derived from Poissonian statistics and error propagation. d/e. The coincidence counts between idler photons and port 1/2 of the Franson interferometer for signal photons for 400 ns storage time. f Each data point is measured for 3 hours, with a constant signal-to-idler ratio, demonstrating the long-term stability of our system.

an efficient, long-storage time and broadband quantum memory $^{8,46-48}$. In our work, we have extended the storage time of entangled photons at telecom wavelength by more than one order of magnitude compared to previous work 42 . Second, we show a successful combination of quantum memory with an integrated quantum-entanglement source, which generates narrow-band entangled photons, is CMOS compatible and hence suitable for scalable fabrication, and easier to use than sources based on bulk optics. Despite these important results, there are several aspects that need to be further improved in our system. For quantum memory, one could use more efficient initialization protocols with a resolved, long-lived hyperfine structure 8,47 , integrated nanostructures enabling stronger light-matter interactions and hence higher memory efficiency 46,48,71,72 . With these experimental improvements, we anticipate $^{167}\text{Er}^{3+}$ ions and integrated quantum photonics to become a versatile platform for high-performance quantum memory, enabling the realization of large-scale quantum networks.

We would like to thank Kaixuan Zhu, Penghong Yu and Xuntao Wu for experimental helps during the early stage of this work. This research is supported by the National Key Research and Development Program of China (2019YFA0308700, 2017YFA0303704), National Natural Science Foundation of China (Grants No.11690032, No.11321063), NSFC-BRICS (No.61961146001), Leading-edge technology Program of Jiangsu Natural Science Foundation (BK20192001), Innovation Program for Quantum Science and Technology (2021ZD0301500), and the Fundamental Research Funds for the Central Universities.

SUPPLEMENTARY INFORMATION

1. Full diagram and time sequence

The full diagram of our experiment is shown in Fig.S1. A continuous wave pump laser (CW1, pump) is chopped by an intensity modulator (IM1) into pulses with a 4-ns pulse duration and a 32-ns period. Then these pulses are further amplified with an Erbium-doped fibre amplifier (EDFA). Two wavelength division multiplexers (WDM) at channel 48 are used to clean the spectrum of the pulses, which are injected into the SiN DMZI-R resonator. Then a pair of frequency non-degenerate photons, signal (1536.17 nm) and idler (1540.87 nm), are generated from the resonator and coupled out from the chip. Signal and idler photons are then separated and filtered with 2 WDMs at channel 45 and channel 51, respectively. The remaining pump pulses are coupled out from the chip and detected with a photodiode (PD). We use the detected power signal to monitor the frequency drift between the resonance of the DMZI-R and the pump. The quantum memory is a ¹⁶⁷Er³⁺:Y₂SiO₅ crystal placed in a dilution refrigerator integrated with a superconducting magnet. To create the AFC, a continuous wave memory laser (CW2, memory) is chopped by an intensity modulator (IM2) into pulses with a 6-ns pulse duration and a period equal to the storage time $t_{\rm M}$. The pump laser and signal photons are focused on the crystal with a waist of about 190 μ m, and propagate through the crystal in opposite directions with an angle of about 1°. A pair of optical shutters is employed to protect the superconducting single photon detectors (SSPD) from the memory laser, with a 3.7-s AFC preparation window, a 1-s memory window, and a 200-ms delay in between. An acousto-optic modulator (AOM) is inserted to gate the idler photons in synchronization with the memory window. The time sequence of the experiment is shown in Fig.S2. Two all-fibre unbalanced Franson interferometers consisting of beam splitters (BS), circulators, fibre stretchers, and Faraday rotator mirrors are built as analyzers for time-bin entanglement. A fraction of the pump laser is injected into the interferometers as a reference to stabilize the phase of Franson interferometers, filtered out later by 3 WDMs at each port, and detected by photodiodes (PD). Two proportional-integral-differential (PID) controllers are employed to stabilize the relative phase. The coincidence between idler and signal photons is detected by SSPDs and analyzed by a time-correlated single photon counting (TCSPC) system. Several fibre polarization controllers (PC) are used to optimize the polarization for respective optical components.

2. Entanglement photon source

The chip-integrated silicon nitride (SiN) dual Mach-Zehnder interferometer resonator (DMZI-R) source is fabricated by advanced SiN fabrication technology (Ligentec). The large band gap of SiN provides ultra-low propagation loss and lower nonlinear loss in the case of high intra-cavity power compared to silicon.

The fibre polarization controller before the two H48 wavelength division multiplexers (WDM) makes sure the light coupled to the chip is in transverse magnetic (TM) mode. The light is coupled into or out from the chip by a V groove fibre array with a pitch of 127 μ m.

Our DMZI-R has a radius of around 230 μm and the free spectral range (FSR) is close to 100 GHz for TM mode. The length difference of the two unbalanced MZIs is about 240 μm and hence the DMZI interference period is about 600 GHz.

The device we use has the following specifications: The gaps between the waveguide to the ring at the In–Through side and Add–Drop side are nominally 500 nm and 450 nm, respectively. The relatively large size of components and the small thermo-optic coefficient of silicon nitride reduce the thermal crosstalk between different thermo-optical phase shifters. The resistors on the In–Through MZI, Add–Drop MZI and the central ring are about 5000, 2600, and 1800 Ohms, respectively. The resistor on the ring, in conjunction with the TEC for the whole chip, tunes the wavelength of the photon pairs to match quantum storage and the relative phase between the different paths of the Add–Drop MZI at the same time.

3. Time correlation of the idler and signal photons

The idler and signal photons are generated simultaneously by a SFWM process, resulting in a defined time correlation. However, the photons are trapped by the MRR cavity and the correlation peak is broadened. The average

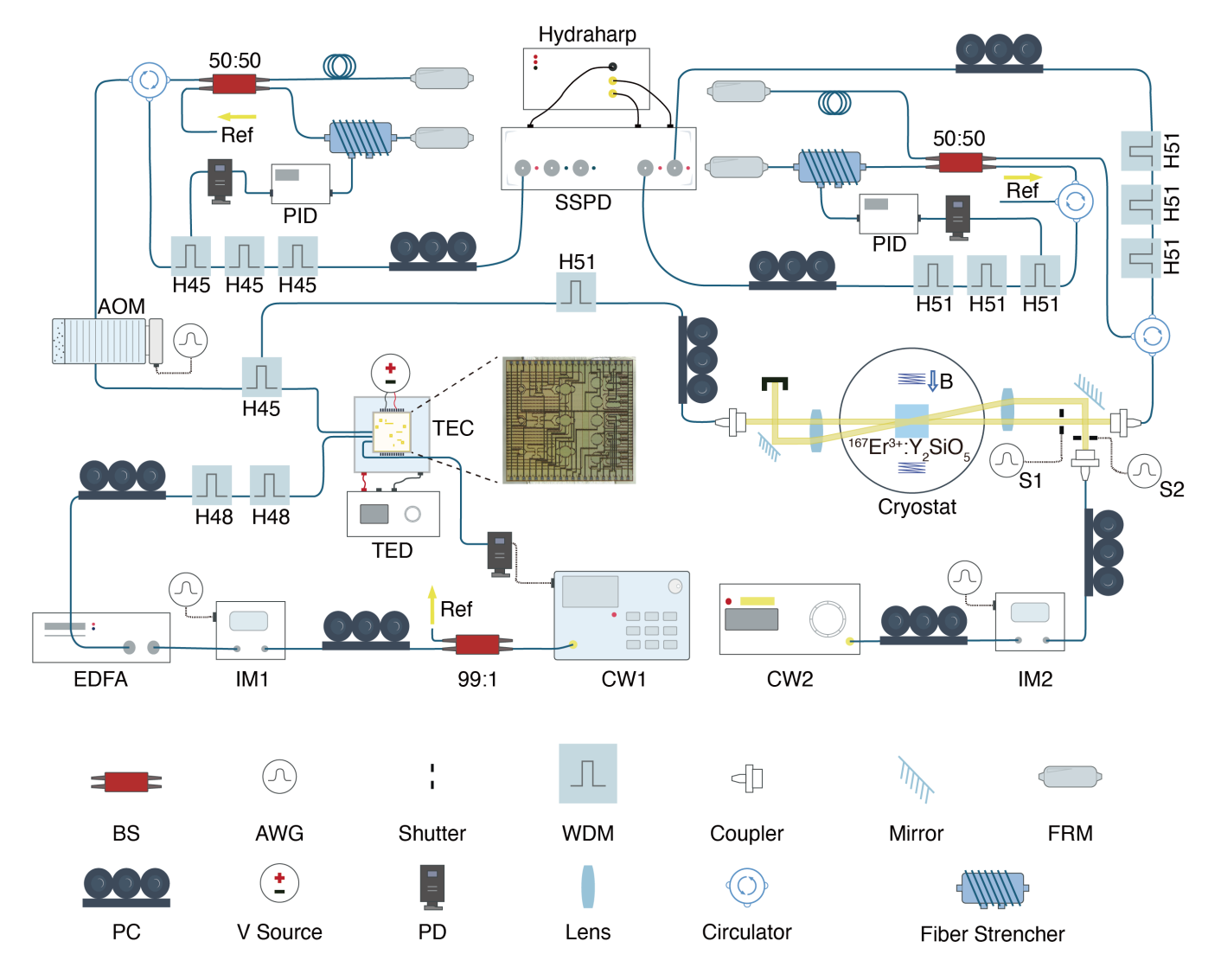


FIG. S1. Full diagram of the experiment. See text for details.

lifetime of photons in a cavity is given by

$$T_{\rm cav} = \frac{1}{2\pi\Delta\nu},\tag{S1}$$

where $\Delta\nu$ is the linewidth of the cavity. The probability that a photon escapes from the cavity with a delay of t after its generation is proportional to $e^{-t/T_{\text{cav}}}$. For an idler-start-and-signal-stop detection, the probability of a coincidence with a time difference of τ is given as below:

$$\tau > 0: \quad p \propto \int_0^\infty e^{-\frac{t}{T_i}} e^{-\frac{t+\tau}{T_s}} dt = e^{-\frac{\tau}{T_s}} \int_0^\infty e^{-\frac{t}{T_i}} e^{-\frac{t}{T_s}} dt = e^{-\frac{\tau}{T_s}} \times \text{const}, \tag{S2a}$$

$$\tau < 0: \quad p \propto \int_0^\infty e^{-\frac{t-\tau}{T_{\rm i}}} e^{-\frac{t}{T_{\rm s}}} dt = e^{\frac{\tau}{T_{\rm i}}} \int_0^\infty e^{-\frac{t}{T_{\rm i}}} e^{-\frac{t}{T_{\rm s}}} dt = e^{\frac{\tau}{T_{\rm i}}} \times \text{const}, \tag{S2b}$$

where $T_{\rm i}$ and $T_{\rm s}$ are the cavity lifetime for the idler and signal photons, respectively. By using this model, we obtain the lifetime for the signal and idler photons to be 342 ps and 555 ps respectively, as presented in the Fig. 2c of the maintext.

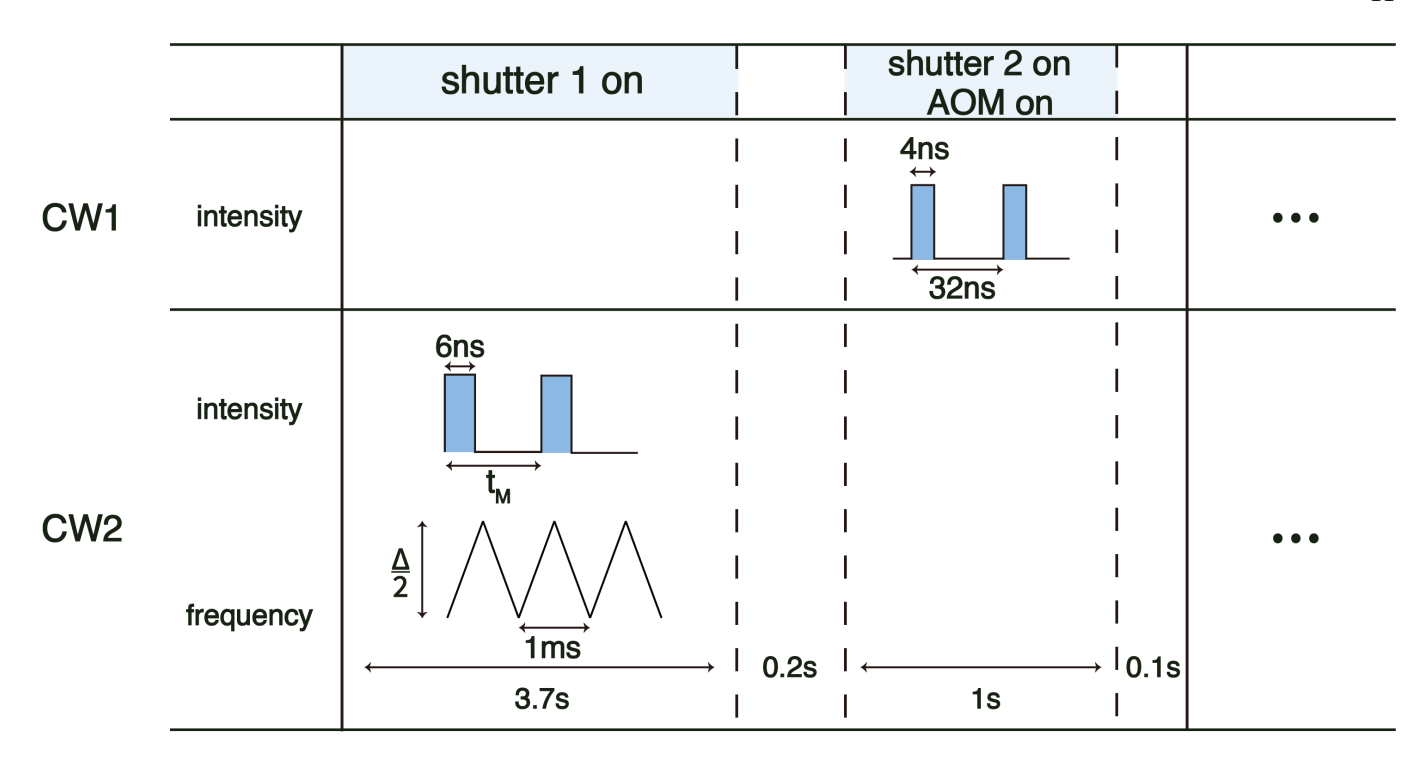


FIG. S2. **Time sequence of the experiment.** The two lasers are chopped by two intensity modulators. The frequency of CW2 is swept with its build-in feature. Two optical shutters separate CW2 and the signal photons temporally.

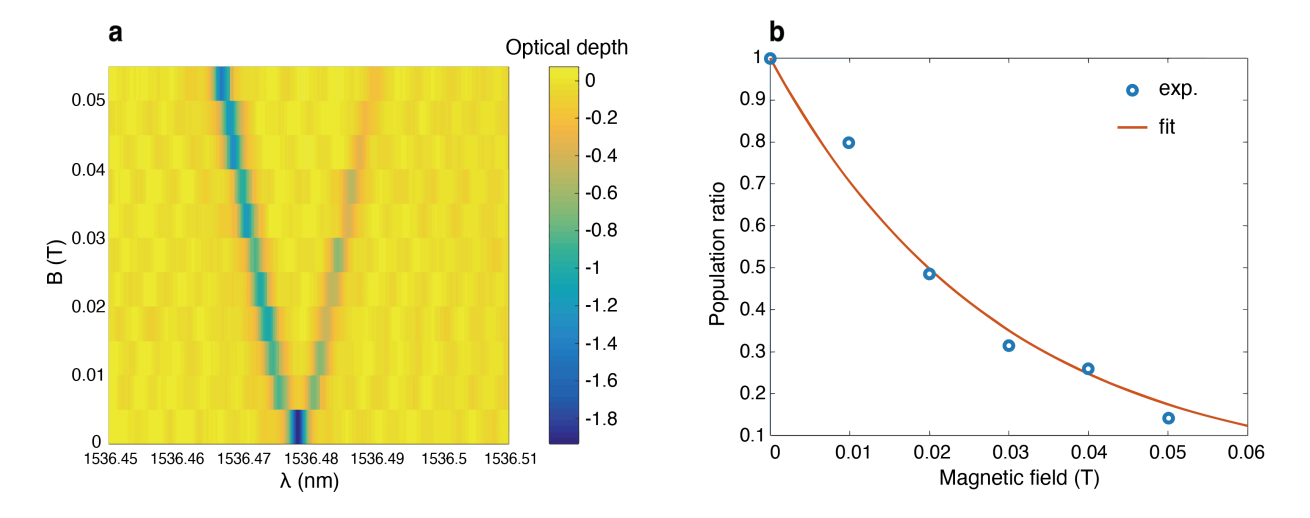


FIG. S3. **Temperature estimation.** a. Zeeman splitting of the non-isotopic Er^{3+} :Y₂SiO₅ crystal. b. The populations ratio between the two Zeeman levels in Fig. S3(a) are extracted, and fit to Boltzmann distribution with T = 200 mK.

4. Details of the crystal and the environment

A 50 ppm doped $^{167}\mathrm{Er}^{3+}$: $Y_2\mathrm{SiO}_5$ $4\times5\times9$ mm³ (D_1,D_2,b) crystal is cooled to about 200 mK in a dilution refrigerator integrated with a superconducting magnet. The temperature of the $^{167}\mathrm{Er}^{3+}$ ensemble is deduced from the thermal-equilibrium population between two ground Zeeman levels at different magnetic fields. The hyperfine states of $^{167}\mathrm{Er}^{3+}$ are not splitted clearly in a low magnetic field. Therefore, we use another 10 ppm doped non-isotopic Er^{3+} : $\mathrm{Y}_2\mathrm{SiO}_5$ crystal to calibrate the temperature under the similar experiment configuration (such as power and beam size), as shown in Fig. S3.

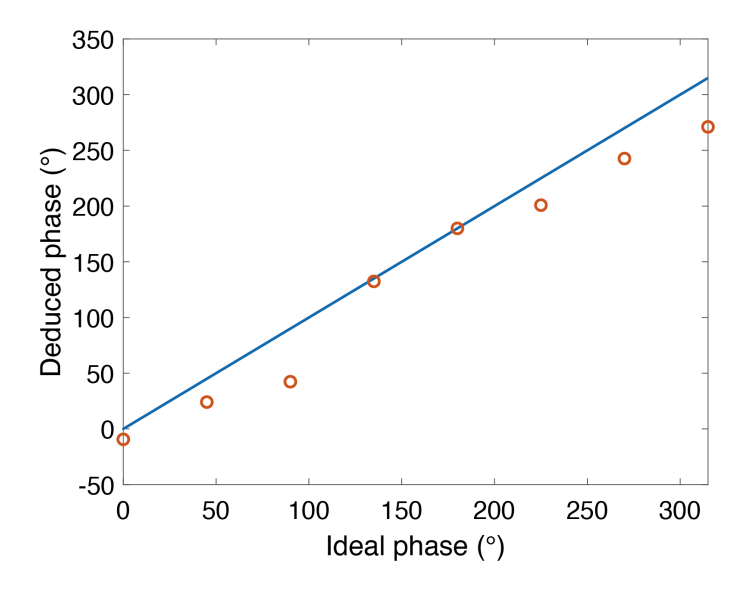


FIG. S4. **Phase tuning of the Franson interferometers.** The ideal phases are determined by the central coincidence peaks. The deduced phases are obtained from the voltage setpoints of PID systems and the maximal/minimal voltages when scanning the interferometers.

	<u> </u>	*	
Phase (°)	U_{idler} (V)	$U_{ m signal}$ (V)	Deduced phase (°)
0	2.2	-1.8	-9.4
45	1.3	-2.3	24.1
90	-3.2	1.4	42.4
135	3.2	3.8	132.4
180	2.4	2.6	180
225	1.8	2.3	200.8
270	1.2	1.2	242.7
315	-0.7	4.2	271.1

TABLE S1. The ideal phase, PID setpoints and the deduced phase of the Franson interferometers.

5. Phase lock of the unbalanced interferometers

In this experiment, the time difference of the unbalanced interferometers is much larger than the coherence time of idler and signal photons, eliminating the single photon interference. The Franson interference of coincidence arises from the coherence of the pump laser, which makes it the natural choice for the reference of the Franson interferometers.

The global phase of the Franson interferometers is locked with PID feedback controllers by using transmission of the pump laser (CW1) as a reference. With PID controllers, we cannot lock the phase of each interferometer to the top or bottom point, but the global phase between the two interferometers can reach the full 2π period. The setpoints are determined by the central coincidence peaks of port 1/2 and the correspondence between the ideal and deduced phases are shown in Fig. S4. The voltage setpoints of each photodetector's output for different phases are shown in Tab. S1, where the sign notes the positive or negative edge of the PID controllers.

^{*} Equal contribution

[†] Xiaosong.Ma@nju.edu.cn

^[1] H. J. Kimble, The quantum internet, Nature 453, 1023 (2008).

^[2] S. Wehner, D. Elkouss, and R. Hanson, Quantum internet: A vision for the road ahead, Science 362, eaam9288 (2018).

^[3] H.-J. Briegel, W. Dür, J. I. Cirac, and P. Zoller, Quantum repeaters: The role of imperfect local operations in quantum communication, Phys. Rev. Lett. 81, 5932 (1998).

- [4] L.-M. Duan, M. D. Lukin, J. I. Cirac, and P. Zoller, Long-distance quantum communication with atomic ensembles and linear optics, Nature 414, 413 (2001).
- [5] C. Simon, H. de Riedmatten, M. Afzelius, N. Sangouard, H. Zbinden, and N. Gisin, Quantum repeaters with photon pair sources and multimode memories, Phys. Rev. Lett. 98, 190503 (2007).
- [6] A. I. Lvovsky, B. C. Sanders, and W. Tittel, Optical quantum memory, Nature Photonics 3, 706 (2009).
- [7] N. Sangouard, C. Simon, H. de Riedmatten, and N. Gisin, Quantum repeaters based on atomic ensembles and linear optics, Rev. Mod. Phys. 83, 33 (2011).
- [8] M. Rančić, M. P. Hedges, R. L. Ahlefeldt, and M. J. Sellars, Coherence time of over a second in a telecom-compatible quantum memory storage material, Nature Physics 14, 50 (2018).
- [9] C.-W. Chou, J. Laurat, H. Deng, K. S. Choi, H. de Riedmatten, D. Felinto, and H. J. Kimble, Functional quantum nodes for entanglement distribution over scalable quantum networks, Science **316**, 1316 (2007).
- [10] Z. S. Yuan, Y. A. Chen, B. Zhao, S. Chen, J. Schmiedmayer, and J. W. Pan, Experimental demonstration of a bdcz quantum repeater node, Nature 454, 1098 (2008).
- [11] A. G. Radnaev, Y. O. Dudin, R. Zhao, H. H. Jen, S. D. Jenkins, A. Kuzmich, and T. A. Kennedy, A quantum memory with telecom-wavelength conversion, Nature Physics 6, 894 (2010).
- [12] Y. Yu, F. Ma, X. Y. Luo, B. Jing, P. F. Sun, R. Z. Fang, C. W. Yang, H. Liu, M. Y. Zheng, X. P. Xie, W. J. Zhang, L. X. You, Z. Wang, T. Y. Chen, Q. Zhang, X. H. Bao, and J. W. Pan, Entanglement of two quantum memories via fibres over dozens of kilometres, Nature 578, 240 (2020).
- [13] Y. F. Pu, S. Zhang, Y. K. Wu, N. Jiang, W. Chang, C. Li, and L. M. Duan, Experimental demonstration of memory-enhanced scaling for entanglement connection of quantum repeater segments, Nature Photonics 15, 374 (2021).
- [14] D. L. Moehring, P. Maunz, S. Olmschenk, K. C. Younge, D. N. Matsukevich, L. M. Duan, and C. Monroe, Entanglement of single-atom quantum bits at a distance, Nature 449, 68 (2007).
- [15] S. Ritter, C. Nölleke, C. Hahn, A. Reiserer, A. Neuzner, M. Uphoff, M. Mücke, E. Figueroa, J. Bochmann, and G. Rempe, An elementary quantum network of single atoms in optical cavities, Nature 484, 195 (2012).
- [16] J. Hofmann, M. Krug, N. Ortegel, L. Gérard, M. Weber, W. Rosenfeld, and H. Weinfurter, Heralded entanglement between widely separated atoms, Science 337, 72 (2012).
- [17] Y. Wang, M. Um, J. Zhang, S. An, M. Lyu, J. N. Zhang, L. M. Duan, D. Yum, and K. Kim, Single-qubit quantum memory exceeding ten-minute coherence time, Nature Photonics 11, 646 (2017).
- [18] I. Usmani, M. Afzelius, H. D. Riedmatten, and N. Gisin, Mapping multiple photonic qubits into and out of one solid-state atomic ensemble, Nature Communications 1, 12 (2010).
- [19] C. Clausen, I. Usmani, F. Bussiéres, N. Sangouard, M. Afzelius, H. D. Riedmatten, and N. Gisin, Quantum storage of photonic entanglement in a crystal, Nature 469, 508 (2011).
- [20] E. Saglamyurek, N. Sinclair, J. Jin, J. A. Slater, D. Oblak, F. Bussìres, M. George, R. Ricken, W. Sohler, and W. Tittel, Broadband waveguide quantum memory for entangled photons, Nature 469, 512 (2011).
- [21] I. Usmani, C. Clausen, F. Bussières, N. Sangouard, M. Afzelius, and N. Gisin, Heralded quantum entanglement between two crystals, Nature Photonics 6, 234 (2012).
- [22] H. Bernien, B. Hensen, W. Pfaff, G. Koolstra, M. S. Blok, L. Robledo, T. H. Taminiau, M. Markham, D. J. Twitchen, L. Childress, and R. Hanson, Heralded entanglement between solid-state qubits separated by three metres, Nature 497, 86 (2013).
- [23] A. Sipahigil, R. E. Evans, D. D. Sukachev, M. J. Burek, J. Borregaard, M. K. Bhaskar, C. T. Nguyen, J. L. Pacheco, H. A. Atikian, C. Meuwly, R. M. Camacho, F. Jelezko, E. Bielejec, H. Park, M. Lončar, and M. D. Lukin, An integrated diamond nanophotonics platform for quantum-optical networks, Science 354, 847 (2016).
- [24] R. Stockill, M. J. Stanley, L. Huthmacher, E. Clarke, M. Hugues, A. J. Miller, C. Matthiesen, C. Le Gall, and M. Atatüre, Phase-tuned entangled state generation between distant spin qubits, Phys. Rev. Lett. 119, 010503 (2017).
- [25] E. Z. Cruzeiro, A. Tiranov, J. Lavoie, A. Ferrier, P. Goldner, N. Gisin, and M. Afzelius, Efficient optical pumping using hyperfine levels in ¹⁴⁵Nd³⁺: Y₂SiO₅ and its application to optical storage, New Journal of Physics **20**, 053013 (2018).
- [26] P. C. Humphreys, N. Kalb, J. P. Morits, R. N. Schouten, R. F. Vermeulen, D. J. Twitchen, M. Markham, and R. Hanson, Deterministic delivery of remote entanglement on a quantum network, Nature 558, 268 (2018).
- [27] A. Wallucks, I. Marinković, B. Hensen, R. Stockill, and S. Gröblacher, A quantum memory at telecom wavelengths, Nature Physics 16, 772 (2020).
- [28] M. Gündoğan, P. M. Ledingham, K. Kutluer, M. Mazzera, and H. de Riedmatten, Solid state spin-wave quantum memory for time-bin qubits, Phys. Rev. Lett. 114, 230501 (2015).
- [29] P. Jobez, C. Laplane, N. Timoney, N. Gisin, A. Ferrier, P. Goldner, and M. Afzelius, Coherent spin control at the quantum level in an ensemble-based optical memory, Phys. Rev. Lett. 114, 230502 (2015).
- [30] K. R. Ferguson, S. E. Beavan, J. J. Longdell, and M. J. Sellars, Generation of light with multimode time-delayed entanglement using storage in a solid-state spin-wave quantum memory, Phys. Rev. Lett. 117, 020501 (2016).
- [31] C. Laplane, P. Jobez, J. Etesse, N. Timoney, N. Gisin, and M. Afzelius, Multiplexed on-demand storage of polarization qubits in a crystal, New Journal of Physics 18, 013006 (2015).
- [32] M. P. Hedges, J. J. Longdell, Y. Li, and M. J. Sellars, Efficient quantum memory for light, Nature 465, 1052 (2010).
- [33] M. Sabooni, Q. Li, S. Kröll, and L. Rippe, Efficient quantum memory using a weakly absorbing sample, Phys. Rev. Lett. 110, 133604 (2013).
- [34] M. Zhong, M. P. Hedges, R. L. Ahlefeldt, J. G. Bartholomew, S. E. Beavan, S. M. Wittig, J. J. Longdell, and M. J. Sellars, Optically addressable nuclear spins in a solid with a six-hour coherence time, Nature 517, 177 (2015).
- [35] Y. Ma, Y. Z. Ma, Z. Q. Zhou, C. F. Li, and G. C. Guo, One-hour coherent optical storage in an atomic frequency comb

- memory, Nature Communications 12, 2381 (2021).
- [36] Y. O. Dudin, A. G. Radnaev, R. Zhao, J. Z. Blumoff, T. A. B. Kennedy, and A. Kuzmich, Entanglement of light-shift compensated atomic spin waves with telecom light, Phys. Rev. Lett. 105, 260502 (2010).
- [37] B. Albrecht, P. Farrera, X. Fernandez-Gonzalvo, M. Cristiani, and H. de Riedmatten, A waveguide frequency converter connecting rubidium-based quantum memories to the telecom c-band, Nature communications 5, 3376 (2014).
- [38] N. Maring, K. Kutluer, J. Cohen, M. Cristiani, M. Mazzera, P. M. Ledingham, and H. de Riedmatten, Storage of upconverted telecom photons in a doped crystal, New Journal of Physics 16, 113021 (2014).
- [39] F. Bussières, C. Clausen, A. Tiranov, B. Korzh, V. B. Verma, S. W. Nam, F. Marsili, A. Ferrier, P. Goldner, H. Herrmann, C. Silberhorn, W. Sohler, M. Afzelius, and N. Gisin, Quantum teleportation from a telecom-wavelength photon to a solid-state quantum memory, Nature Photonics 8, 775 (2014).
- [40] W. Zhang, D.-S. Ding, S. Shi, Y. Li, Z.-Y. Zhou, B.-S. Shi, and G.-C. Guo, Storing a single photon as a spin wave entangled with a flying photon in the telecommunication bandwidth, Phys. Rev. A 93, 022316 (2016).
- [41] A. Seri, A. Lenhard, D. Rieländer, M. Gündoğan, P. M. Ledingham, M. Mazzera, and H. de Riedmatten, Quantum correlations between single telecom photons and a multimode on-demand solid-state quantum memory, Phys. Rev. X 7, 021028 (2017).
- [42] E. Saglamyurek, J. Jin, V. B. Verma, M. D. Shaw, F. Marsili, S. W. Nam, D. Oblak, and W. Tittel, Quantum storage of entangled telecom-wavelength photons in an erbium-doped optical fibre, Nature Photonics 9, 83 (2015).
- [43] E. Saglamyurek, M. Grimau Puigibert, Q. Zhou, L. Giner, F. Marsili, V. B. Verma, S. Woo Nam, L. Oesterling, D. Nippa, D. Oblak, et al., A multiplexed light-matter interface for fibre-based quantum networks, Nature communications 7, 1 (2016).
- [44] M. F. Askarani, M. G. Puigibert, T. Lutz, V. B. Verma, M. D. Shaw, S. W. Nam, N. Sinclair, D. Oblak, and W. Tittel, Storage and reemission of heralded telecommunication-wavelength photons using a crystal waveguide, Phys. Rev. Applied 11, 054056 (2019).
- [45] B. Lauritzen, J. Minář, H. de Riedmatten, M. Afzelius, N. Sangouard, C. Simon, and N. Gisin, Telecommunication-wavelength solid-state memory at the single photon level, Phys. Rev. Lett. 104, 080502 (2010).
- [46] I. Craiciu, M. Lei, J. Rochman, J. M. Kindem, J. G. Bartholomew, E. Miyazono, T. Zhong, N. Sinclair, and A. Faraon, Nanophotonic quantum storage at telecommunication wavelength, Phys. Rev. Applied 12, 024062 (2019).
- [47] J. S. Stuart, M. Hedges, R. Ahlefeldt, and M. Sellars, Initialization protocol for efficient quantum memories using resolved hyperfine structure, Phys. Rev. Research 3, L032054 (2021).
- [48] D.-C. Liu, P.-Y. Li, T.-X. Zhu, L. Zheng, J.-Y. Huang, Z.-Q. Zhou, C.-F. Li, and G.-C. Guo, On-demand storage of photonic qubits at telecom wavelengths, Phys. Rev. Lett. 129, 210501 (2022).
- [49] X. Li, P. L. Voss, J. E. Sharping, and P. Kumar, Optical-fiber source of polarization-entangled photons in the 1550 nm telecom band, Phys. Rev. Lett. **94**, 053601 (2005).
- [50] S. Ramelow, A. Farsi, S. Clemmen, D. Orquiza, K. Luke, M. Lipson, and A. L. Gaeta, Silicon-nitride platform for narrow-band entangled photon generation, arXiv, arXiv:1508.04358 (2015).
- [51] J. A. Jaramillo-Villegas, P. Imany, O. D. Odele, D. E. Leaird, Z.-Y. Ou, M. Qi, and A. M. Weiner, Persistent energy-time entanglement covering multiple resonances of an on-chip biphoton frequency comb, Optica 4, 655 (2017).
- [52] M. Kues, C. Reimer, J. M. Lukens, W. J. Munro, A. M. Weiner, D. J. Moss, and R. Morandotti, Quantum optical microcombs, Nature Photonics 13, 170 (2019).
- [53] X. Lu, Q. Li, D. A. Westly, G. Moille, A. Singh, V. Anant, and K. Srinivasan, Chip-integrated visible–telecom entangled photon pair source for quantum communication, Nature Physics 15, 373 (2019).
- [54] F. Samara, A. Martin, C. Autebert, M. Karpov, T. J. Kippenberg, H. Zbinden, and R. Thew, High-rate photon pairs and sequential Time-Bin entanglement with Si₃N₄ microring resonators, Opt. Express **27**, 19309 (2019).
- [55] F. Samara, N. Maring, A. Martin, A. S. Raja, T. J. Kippenberg, H. Zbinden, and R. Thew, Entanglement swapping between independent and asynchronous integrated photon-pair sources, Quantum Science and Technology 6, 045024 (2021).
- [56] W. Wen, Z. Chen, L. Lu, W. Yan, W. Xue, P. Zhang, Y. Lu, S. Zhu, and X.-s. Ma, Realizing an entanglement-based multiuser quantum network with integrated photonics, Phys. Rev. Applied 18, 024059 (2022).
- [57] Z. Vernon, M. Menotti, C. C. Tison, J. A. Steidle, M. L. Fanto, P. M. Thomas, S. F. Preble, A. M. Smith, P. M. Alsing, M. Liscidini, and J. E. Sipe, Truly unentangled photon pairs without spectral filtering, Opt. Lett. 42, 3638 (2017).
- [58] C. C. Tison, J. A. Steidle, M. L. Fanto, Z. Wang, N. A. Mogent, A. Rizzo, S. F. Preble, and P. M. Alsing, Path to increasing the coincidence efficiency of integrated resonant photon sources, Opt. Express 25, 33088 (2017).
- [59] C. Wu, Y. W. Liu, X. W. Gu, X. X. Yu, Y. C. Kong, Y. Wang, X. G. Qiang, J. J. Wu, Z. H. Zhu, X. J. Yang, and P. Xu, Bright photon-pair source based on a silicon dual-mach-zehnder microring, Science China: Physics, Mechanics and Astronomy 63, 220362 (2020).
- [60] L. Lu, L. Xia, Z. Chen, L. Chen, T. Yu, T. Tao, W. Ma, Y. Pan, X. Cai, Y. Lu, S. Zhu, and X. S. Ma, Three-dimensional entanglement on a silicon chip, npj Quantum Information 6, 30 (2020).
- [61] Z.-Y. Zhou, D.-S. Ding, Y. Li, F.-Y. Wang, and B.-S. Shi, Cavity-enhanced bright photon pairs at telecom wavelengths with a triple-resonance configuration, J. Opt. Soc. Am. B 31, 128 (2014).
- [62] C. Reimer, L. Caspani, M. Clerici, M. Ferrera, M. Kues, M. Peccianti, A. Pasquazi, L. Razzari, B. E. Little, S. T. Chu, D. J. Moss, and R. Morandotti, Integrated frequency comb source of heralded single photons, Opt. Express 22, 6535 (2014).
- [63] J. D. Franson, Bell inequality for position and time, Phys. Rev. Lett. 62, 2205 (1989).
- [64] J. F. Clauser, M. A. Horne, A. Shimony, and R. A. Holt, Proposed experiment to test local hidden-variable theories, Phys. Rev. Lett. 23, 880 (1969).
- [65] M. Afzelius, C. Simon, H. de Riedmatten, and N. Gisin, Multimode quantum memory based on atomic frequency combs,

- Phys. Rev. A 79, 052329 (2009).
- [66] P. R. Tapster and J. G. Rarity, Photon statistics of pulsed parametric light, Journal of Modern Optics 45, 595 (1998).
- [67] S. Fasel, O. Alibart, S. Tanzilli, P. Baldi, A. Beveratos, N. Gisin, and H. Zbinden, High-quality asynchronous heralded single-photon source at telecom wavelength, New Journal of Physics 6, 163 (2004).
- [68] X. Zheng, P. Zhang, R. Ge, L. Lu, G. He, Q. Chen, F. Qu, L. Zhang, X. Cai, Y. Lu, et al., Heterogeneously integrated, superconducting silicon-photonic platform for measurement-device-independent quantum key distribution, Advanced Photonics 3, 055002 (2021).
- [69] O. Gühne and G. Tóth, Entanglement detection, Physics Reports 474, 1 (2009).
- [70] X. Liu, J. Hu, Z. F. Li, X. Li, P. Y. Li, P. J. Liang, Z. Q. Zhou, C. F. Li, and G. C. Guo, Heralded entanglement distribution between two absorptive quantum memories, Nature **594**, 41 (2021).
- [71] A. Seri, D. Lago-Rivera, A. Lenhard, G. Corrielli, R. Osellame, M. Mazzera, and H. de Riedmatten, Quantum storage of frequency-multiplexed heralded single photons, Phys. Rev. Lett. 123, 080502 (2019).
- [72] M. Raha, S. Chen, C. M. Phenicie, S. Ourari, A. M. Dibos, and J. D. Thompson, Optical quantum nondemolition measurement of a single rare earth ion qubit, Nature Communications 11, 1605 (2020).